AGU PUBLICATIONS

JGR

Journal of Geophysical Research: Oceans

RESEARCH ARTICLE

10.1002/2017JC013267

Special Section:
Sea State and Boundary Layer Physics of the Emerging Arctic Ocean

Large Eddy Simulation of Heat Entrainment Under Arctic Sea Ice

Eshwan Ramudu[1], Renske Gelderloos[1], Di Yang[2], Charles Meneveau[3], and Anand Gnanadesikan[1]

[1]Department of Earth and Planetary Sciences, Johns Hopkins University, Baltimore, MD, USA, [2]Department of Mechanical Engineering, University of Houston, Houston, TX, USA, [3]Department of Mechanical Engineering, Johns Hopkins University, Baltimore, MD, USA

Key Points:
- Turbulence caused by drifting sea ice in the Canada Basin does not entrain heat from the Pacific Summer Water layer
- The presence of the Near-Surface Temperature Maximum layer enhances heat entrainment from the mixed layer
- Heat delivery is super-linear in the ice-drift velocity and sublinear in the temperature forcing

Supporting Information:
- Supporting Information S1

Correspondence to:
A. Gnanadesikan,
gnanades@jhu.edu

Citation:
Ramudu, E., Gelderloos, R., Yang, D., Meneveau, C., & Gnanadesikan, A. (2018). Large eddy simulation of heat entrainment under Arctic Sea Ice. *Journal of Geophysical Research: Oceans*, *123*. https://doi.org/10.1002/2017JC013267

Received 13 JUL 2017
Accepted 20 DEC 2017
Accepted article online 28 DEC 2017

Abstract Arctic sea ice has declined rapidly in recent decades. The faster than projected retreat suggests that free-running large-scale climate models may not be accurately representing some key processes. The small-scale turbulent entrainment of heat from the mixed layer could be one such process. To better understand this mechanism, we model the Arctic Ocean's Canada Basin, which is characterized by a perennial anomalously warm Pacific Summer Water (PSW) layer residing at the base of the mixed layer and a summertime Near-Surface Temperature Maximum (NSTM) within the mixed layer trapping heat from solar radiation. We use large eddy simulation (LES) to investigate heat entrainment for different ice-drift velocities and different initial temperature profiles. The value of LES is that the resolved turbulent fluxes are greater than the subgrid-scale fluxes for most of our parameter space. The results show that the presence of the NSTM enhances heat entrainment from the mixed layer. Additionally there is no PSW heat entrained under the parameter space considered. We propose a scaling law for the ocean-to-ice heat flux which depends on the initial temperature anomaly in the NSTM layer and the ice-drift velocity. A case study of "The Great Arctic Cyclone of 2012" gives a turbulent heat flux from the mixed layer that is approximately 70% of the total ocean-to-ice heat flux estimated from the PIOMAS model often used for short-term predictions. Present results highlight the need for large-scale climate models to account for the NSTM layer.

1. Introduction

The Arctic sea ice cover has been decreasing over the past few decades (Johannessen et al., 1999; Kwok & Rothrock, 2009; Meier, 2017). This trend can severely affect Earth's climate by causing the Arctic region to continue warming through the positive ice-albedo feedback mechanism as well as by influencing weather and circulation patterns in the midlatitudes. It can also significantly impact animals, plants, and human activity in and near the Arctic (Notz & Stroeve, 2016). The decline in Arctic sea ice is occurring faster than predicted by global climate models (Kirchmeier-Young et al., 2017; Stroeve et al., 2007), which leads to questions about whether these models are missing some key mechanisms responsible for the melting of sea ice. One such mechanism could be the supply of heat by entrainment from the upper ocean to the ice-ocean interface. In this study, we explore heat entrainment under drifting sea ice during the summertime in order to better understand this process and its contribution to Arctic sea ice melt.

We focus our study on the Canada Basin in the Arctic Ocean, located roughly between latitudes 72°N and 84°N and longitudes 157°W and 128°W. Among the six regions of the Arctic, the Canada Basin experienced the second largest sea ice thickness decrease rate between 2002 and 2007 (Kwok & Rothrock, 2009). The structure of the upper water column in the Canada Basin is illustrated in Figure 1. We define the ocean mixed layer as being the layer at the top bounded by a strong density gradient (and hence by a strong salinity gradient, since in the Arctic density is primarily influenced by salinity) below. The mixed layer may be thought of as a layer which experiences mixing at some point during the year, thus being distinguished from a mixing layer which is a layer whose depth corresponds to the depth of active mixing at any one time. The Canada Basin consists of a shallow mixed layer about 40 m deep (Toole et al., 2010). Warm water of Pacific origin circulates at the base of the mixed layer (Coachman & Barnes, 1961; Steele et al., 2004) and the heat content of this so-called Pacific Summer Water has been increasing over the years (Timmermans et al., 2014; Woodgate et al., 2006). The mixed layer and PSW layer are separated by a pycnocline that is

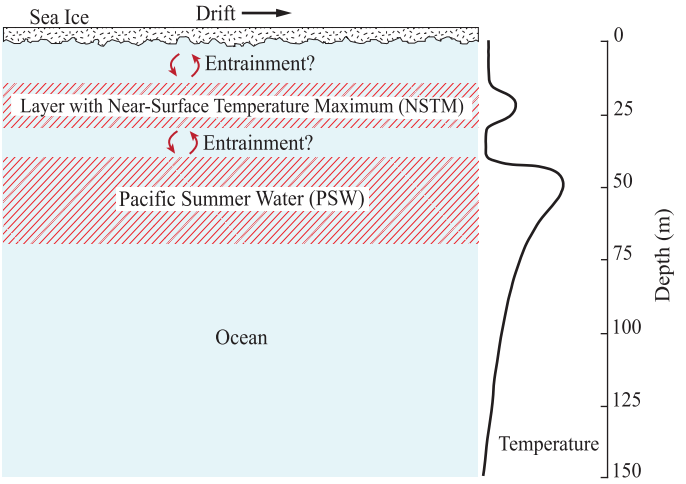

Figure 1. Schematic of the typical vertical structure and temperature profile in the Canada Basin in the Arctic Ocean.

strongly salinity-stratified (Toole et al., 2010). Within the mixed layer, a Near-Surface Temperature Maximum layer (NSTM) often forms during the summer as a result of solar radiation penetrating through open water areas and getting stored near the surface (McPhee et al., 1998). Given the trend of decreasing sea ice and earlier melt dates in the summer, it is likely that the NSTM will become warmer in time (Jackson et al., 2010).

Several studies have investigated the influences of the heat-containing PSW and NSTM layers on sea ice. Shimada et al. (2006) noted that the spatial distribution of the decrease of sea ice concentration corresponds to the spatial distribution of PSW and that the sharper decline in sea ice concentration in the late 1990s coincided with the warming trend of the PSW. Woodgate et al. (2010) suggested that the heat flux carried by the flow of PSW into the Arctic initiates the seasonal melting and the formation of open water areas in the sea ice cover. Using observations taken underneath a drifting ice floe in the Beaufort Gyre from the Surface Heat Budget of the Arctic Ocean (SHEBA) project, Shaw et al. (2009) estimated the upward heat flux across the pynocline to be 0.1–1.5 W m^{-2} and the ice-ocean heat flux to be about 16.3 W m^{-2} during the summer warming season. Their concurrent numerical modeling indicated a very small heat entrained from the pycnocline, which showed that the heat for sea ice melting primarily came from solar radiation stored within the mixed layer. On the basis of observations in the Canada Basin in the time period 2004–2009 and of simulation results using a one-dimensional mixed layer, Toole et al. (2010) argued that the pycnocline is so stable due to its stratification that PSW heat remains confined underneath the mixed layer. Steele et al. (2010) analyzed the summertime heat budget of the surface layer (0–60 m) of the Canada Basin with the Pan-Arctic Ice-Ocean Modeling and Assimilation System (PIOMAS) and found that heat flux from the atmosphere accounts for 77–83% of the warming of the upper ocean while the heat flux from the PSW layer is relatively very small. None of the modeling studies among these prior studies, however, resolved the turbulence explicitly.

In this study, we use large eddy simulation (LES) to investigate the turbulent transport of heat from the PSW and NSTM layers to the basal surface of sea ice as it drifts over the surface of the ocean. Unlike climate models which rely entirely on parameterizations of turbulent diffusion, LES is able to explicitly resolve turbulent fluxes down to the grid scale, with only the subgrid-scale (SGS) component requiring parameterization. Considering that the contribution of turbulent heat entrainment to bottom melting of sea ice is currently a key question in Arctic oceanography, we choose to use LES to help improve our understanding of this physical process as LES can capture the details of the turbulent heat fluxes. In turn, this can provide useful insights for developing more accurate parameterizations for climate models. Our LES model is based on a high-fidelity spectral approach on horizontal planes and utilizes a scale-dependent Lagrangian SGS model that dynamically calculates the model coefficients for SGS quantities without ad hoc tuning. We remark that Skyllingstad and Denbo (2001) also used LES, coupled with an ice model, to investigate the ice-ocean boundary layer. While their work focused on the case of wintertime freezing, ours applies to summertime melting. Additionally, we do not couple our LES model with an ice model for reasons explained in section 2. We do, however, include the impact of sea ice melt on temperature and salinity via the surface boundary conditions.

Our study isolates the effect of the shear stress-induced turbulence under moving sea ice on heat entrainment from the mixed layer. It can thus show what fraction of observed sea ice melt is due to heat contained in the ocean. To ensure a realistic range of ice-drift velocities, we calculated the observed range from the recorded hourly locations of Ice-Tethered Profilers (ITPs) (Krishfield et al., 2008; Toole et al., 2010) deployed in the Canada Basin since 2005 (Figure 2). Based on these observations, the velocities considered in this study are 0.03–0.30 m s^{-1}.

This paper is organized as follows. Section 2 describes in detail the approach and the setup of the numerical model. In section 3, results from simulations investigating the interaction of moving sea ice with the warm PSW and NSTM layers are presented. A case study of the effect of an intense 2012 Arctic cyclone on heat

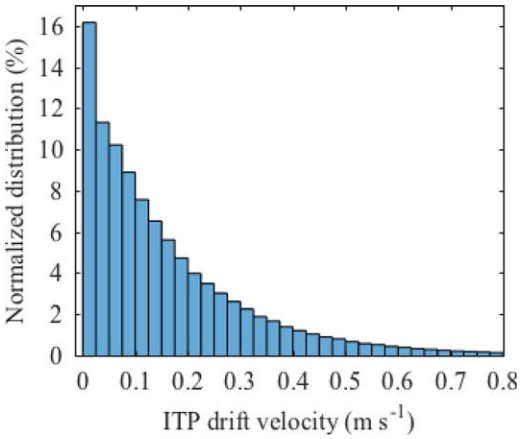

Figure 2. Histogram of ice-drift velocities of ITPs deployed in the Canada Basin since 2005 (records used are from ITP 1, 2, 3, 4, 5, 6, 8, 11, 13, 18, 21, 23, 32, 33, 34, 41, 42, 43, 52, 55, 69, 77, 78, 79, 80, 82, 84, 85, 86, 87).

entrainment from the ocean with the LES model is conducted in section 4. Finally, the results are summarized in section 5.

2. Numerical Model

2.1. Governing Equations

The LES model solves the three-dimensional equations governing the flow under an ice-ocean interface:

$$\frac{\partial \widetilde{u}_i}{\partial t}+\widetilde{u}_j\frac{\partial \widetilde{u}_i}{\partial \widetilde{x}_j}=-\frac{\partial \widetilde{p}}{\partial x_i}+\epsilon_{ij3}f\widetilde{u}_j-\delta_{i3}g\left(1-\frac{\widetilde{\rho}(\widetilde{\theta},\widetilde{S})}{\rho_0}\right)-\frac{\partial \tau_{ij}}{\partial x_j} \quad (1)$$

$$\frac{\partial \widetilde{u}_i}{\partial x_i}=0 \quad (2)$$

$$\frac{\partial \widetilde{\theta}}{\partial t}+\widetilde{u}_i\frac{\partial \widetilde{\theta}}{\partial x_i}=-\frac{\partial q_{T,i}}{\partial x_i} \quad (3)$$

$$\frac{\partial \widetilde{S}}{\partial t}+\widetilde{u}_i\frac{\partial \widetilde{S}}{\partial x_i}=-\frac{\partial q_{S,i}}{\partial x_i} \quad (4)$$

(1) is the momentum equation in which the Boussinesq approximation is made, (2) is the continuity equation, and (3) and (4) are the advection-diffusion equations for the scalars potential temperature θ and absolute salinity S, respectively. In these equations, the tilde, $\widetilde{(..)}$, refers to a variable filtered on the LES grid and i and j are indices which can take the values 1, 2, and 3 to denote the directions x, y, and z respectively. u_i is the velocity, and u_1 and u_2 will be denoted by u and v respectively; t is time; p is the kinematic pressure; f is the Coriolis parameter; g is the acceleration due to gravity; ρ is the potential density; ρ_0 is a reference density; $\tau_{ij}=\widetilde{u_iu_j}-\widetilde{u}_i\widetilde{u}_j$ is the SGS stress tensor; $q_{T,i}=\widetilde{u_i\theta}-\widetilde{u}_i\widetilde{\theta}$ is the SGS heat flux; and $q_{S,i}=\widetilde{u_iS}-\widetilde{u}_i\widetilde{S}$ is the SGS salt flux. (1)–(4) form a coupled system. We use the nonlinear equation of state for seawater (TEOS-10) to obtain the potential density $\widetilde{\rho}$ based on the potential temperature $\widetilde{\theta}$ and absolute salinity $\widetilde{S}$ (IOC et al., 2010). Since the Reynolds number of the flow is very high, the effects of molecular viscosity and molecular thermal and salt diffusion are negligible and thus not included in the model. The values and units of all the constants used are listed in Table 1. The equations are discretized on a Cartesian grid to solve for the velocity components and the evolution of the potential temperature and absolute salinity fields. The dimensions of the domain are $L_x=L_y=300$ m and $L_z=150$ m and the corresponding numbers of computational grid points are $N_x=N_y=128$ and $N_z=257$. The grid sizes $\Delta_x=L_x/N_x$, $\Delta_y=L_y/N_y$, and $\Delta_z=L_z/(N_z-1)$ are uniform in each direction.

2.2. Numerical Implementation

The LES model is based on the work of Albertson and Parlange (1999). It has since been tested and used extensively with application to the atmospheric boundary layer (Calaf et al., 2011; Kumar et al., 2006; Porté-Agel, 2004) and the ocean surface layer (Yang et al., 2014, 2015). In the model, the horizontal components of velocity, the pressure, and the scalar quantities are stored at the cell center. The vertical velocity is stored on a grid staggered in the vertical direction by $\Delta z/2$. Derivatives on the horizontal plane are computed using spectral methods while derivatives on the vertical plane are approximated using second-order finite difference. In the momentum equation, the nonlinear term is computed in rotational form to help ensure the conservation of mass and kinetic energy (Orszag & Pao, 1975). The momentum equation is solved by the projection method. In this procedure, an intermediate velocity field is first obtained by integrating the momentum equation to an intermediate time step without the pressure gradient term. A Poisson equation for the pressure is then solved using the pipelined Thomas algorithm (Povitsky & Morris, 2000). Finally, the intermediate velocity field is integrated to the new time step with a pressure correction to obtain the new velocity field. Time integration in the momentum equation and scalar transport equations is performed using the second-order Adams-Bashforth method. In order to avoid aliasing errors, the nonlinear terms are dealiased using the 3/2 rule (Canuto et al., 1988). The model is parallelized using Message Passing Interface (MPI).

Table 1
Constants Used in Model

Property	Symbol	Units	Value
Specific heat capacity of ice	c_{ice}	J kg^{-1} K^{-1}	2.10×10^{3}[b]
Specific heat capacity of seawater	c_ℓ	J kg^{-1} K^{-1}	4.02×10^{3}[a]
Coriolis parameter	f	s^{-1}	1.45×10^{-4}
Acceleration due to gravity	g	m s^{-2}	9.81
Molecular salt diffusivity of seawater	k_S	m^2 s^{-1}	9.0×10^{-10}[b]
Molecular thermal diffusivity of seawater	k_T	m^2 s^{-1}	1.38×10^{-7}[a]
Latent heat of fusion of seawater	L	J kg^{-1}	$L_f(1-0.03S_{ice})$[d]
Latent heat of fusion of fresh water	L_f	J kg^{-1}	3.35×10^{5}[b]
Constant relating freezing temperature to ocean salinity	m	°C psu^{-1}	0.054[f]
Typical salinity of sea ice	S_{ice}	g kg^{-1}	3[c]
Basal roughness length at ITP 77 on 14 June 2014	z_0	m	1.2×10^{-5}[e]
Thermal expansion coefficient of seawater	α	°C^{-1}	2×10^{-4}
von Karman constant	κ		0.4
Kinematic viscosity of seawater	ν	m^2 s^{-1}	1.84×10^{-6}[a]
Reference density of seawater	ρ_0	kg m^{-3}	1024[a]
Reference density of sea ice	ρ_{ice}	kg m^{-3}	917[b]

[a]Sharqawy et al. (2010).
[b]Kantha and Clayson (2000).
[c]IOC et al. (2010).
[d]McPhee (2008).
[e]Cole et al. (2017).
[f]UNESCO (1981).

2.3. SGS Model

The expression for the (deviatoric part of the) SGS stress tensor in (1) is based on the Smagorinsky model (Smagorinsky, 1963):

$$\tau_{ij} = -2\nu_t \widetilde{\mathcal{S}}_{ij} \tag{5}$$

$\mathcal{S}$ is the strain-rate tensor and ν_t is the eddy viscosity, which is itself given by $\nu_t = (C_s\Delta)^2|\widetilde{\mathcal{S}}|$, where C_s is the Smagorinsky coefficient and $\Delta = (\Delta_x\Delta_y\Delta_z)^{1/3}$ is the cutoff filter size in the LES. C_s is evaluated using the scale-dependent Lagrangian dynamic model of Bou-Zeid et al. (2005). Through the use of Lagrangian averaging over fluid pathlines, this method is able to capture the statistically significant spatial and temporal variation in C_s and remain stable at the same time (Meneveau et al., 1996). By being scale-dependent, it is well-suited for LES of inhomogeneous high Reynolds number boundary layer flows where scale-dependence of C_s is expected (Bou-Zeid et al., 2005), as is the case in this study. Furthermore, in this model, C_s is determined directly using resolved quantities, so that there is no need for empirical inputs or a priori tuning. The SGS heat flux $q_{T,i}$ and SGS salt flux $q_{S,i}$ are modeled as

$$q_{T,i} = -K_T \frac{\partial\widetilde{\theta}}{\partial x_i} \text{ and} \tag{6}$$

$$q_{S,i} = -K_S \frac{\partial\widetilde{S}}{\partial x_i}, \tag{7}$$

where K_T is the SGS thermal eddy diffusivity and K_S is the SGS salt eddy diffusivity. They are evaluated as $K_T = \nu_t/\mathrm{Pr}_{SGS}$ and $K_S = \nu_t/\mathrm{Sc}_{SGS}$, where $\mathrm{Pr}_{SGS}=0.4$ is the turbulent SGS Prandtl number (Antonopoulos-Domis, 1981; Mason, 1989; Yang et al., 2015) and $\mathrm{Sc}_{SGS}=0.6$ is the turbulent SGS Schmidt number (Skyllingstad et al., 1999).

2.4. Boundary Conditions

At the basal ice surface (ice-ocean interface), where $z = 0$, the ocean water moves at a prescribed velocity U_b, the effect of a virtual ice cover over the whole domain drifting at a constant velocity in the x direction. Hence, U_b is also referred to as the ice velocity. We ignore the vertical motion of the basal ice surface due to

melting as well as convergent or divergent ice motions in our simulations. Based on the Monin-Obukhov similarity law, the resulting shear stress τ_{i3} ($i = 1, 2$) at the top is expressed as

$$\tau_{i3} = -u_*^2 \left[\frac{\widehat{\widehat{u}}_{r,i}(z_1)}{\sqrt{\widehat{\widehat{u}}_{r,1}^2(z_1) + \widehat{\widehat{u}}_{r,2}^2(z_1)}} \right] \tag{8}$$

where

$$\widehat{\widehat{u}}_{r,i}(z_1) = \begin{cases} \widehat{\widehat{u}}_i(z_1) - U_b, & i=1 \\ \widehat{\widehat{u}}_i(z_1), & i=2 \end{cases} \tag{9}$$

and u_* is the friction velocity given by

$$u_* = \frac{\sqrt{\widehat{\widehat{u}}_{r,1}^2(z_1) + \widehat{\widehat{u}}_{r,2}^2(z_1)}}{(1/\kappa)\ln(z_1/z_0)} \tag{10}$$

$\kappa = 0.4$ is the von Karman constant, $z_1 = \Delta z/2$ is the vertical distance of the first computational grid point, and z_0 is the roughness length of the basal ice surface. The hat, $\widehat{(..)}$, denotes test-filtering of the variables at a scale 2Δ, which is done to reduce small-scale fluctuations between the local points at which the Monin-Obukhov similarity law is applied such that the large-scale fluctuations have greater influence on the solution (Bou-Zeid et al., 2005). The boundary conditions in the horizontal directions are periodic. At the bottom of the domain, a stress-free condition is imposed. To prevent reflection of gravity waves from the bottom, vertical velocities are damped using a sponge layer (Nieuwstadt et al., 1993).

The boundary conditions for temperature and salinity at the top are derived by considering the heat and salt balances at the virtual ice-ocean interface, following the procedure of Skyllingstad and Denbo (2001). Denoting $q_{T,3}$ and $q_{S,3}$ at $z = 0$ by q_{T*} and q_{S*},

$$\rho_{\text{ice}} L W_b = \rho_0 c_\ell q_{T*} - \rho_{\text{ice}} c_{\text{ice}} q_{\text{ice}} \tag{11}$$

$$(S_b - S_{\text{ice}}) W_b = q_{S*} \tag{12}$$

L is the latent heat of fusion sea ice; W_b, the vertical velocity of the ice-ocean interface; c_ℓ, the specific heat capacity of seawater; c_{ice}, the specific heat capacity of sea ice; q_{ice}, the heat flux through the ice; S_b, the salinity of the ocean at the ice-ocean interface; and S_{ice}, the salinity in the interior of sea ice. When ice is melting in the summer, which is the case we consider in this study, $q_{\text{ice}} \ll q_{T*}$ (Shaw et al., 2009), so the second term on the right-hand side of (11) can be neglected. The fluxes q_{T*} and q_{S*} are formulated using Monin-Obukhov similarity theory as

$$q_{T*} = \frac{1}{\Phi_T} [\widehat{\theta}(z_1) - \theta_b] u_* \tag{13}$$

$$q_{S*} = \frac{1}{\Phi_T} [\widehat{S}(z_1) - S_b] u_* \tag{14}$$

where θ_b is the freezing temperature at the ice-ocean interface. We adopt the expressions of McPhee et al. (1987) and Skyllingstad and Denbo (2001) for Φ_T and Φ_S in (13) and (14), respectively:

$$\Phi_T = \frac{1}{\kappa} \ln\left(\frac{z_1}{z_0}\right) + 1.57 \left(\frac{u_* z_0}{\nu}\right)^{1/2} \left(\frac{\nu}{k_T}\right)^{2/3} \tag{15}$$

$$\Phi_S = \frac{1}{\kappa} \ln\left(\frac{z_1}{z_0}\right) + 1.57 \left(\frac{u_* z_0}{\nu}\right)^{1/2} \left(\frac{\nu}{k_S}\right)^{2/3} \tag{16}$$

In the above expressions, ν is the molecular viscosity, k_T is the molecular thermal diffusivity, and k_S is the molecular salt diffusivity of sea water. θ_b and S_b are unknown quantities in (13) and (14), respectively. The use of $\theta_b = -mS_b$, where $m = 0.054$°C psu^{-1} (UNESCO, 1981), in (13) and the substitution of the resulting expression as well as of (14) in (11) and (12) yield a quadratic equation for S_b:

$$mS_b^2+\left[\widehat{\widehat{\theta}}(z_1)-mS_{\text{ice}}+\frac{\Phi_T L}{\Phi_S}\right]S_b-\left[\widehat{\widehat{\theta}}(z_1)S_{\text{ice}}+\frac{\Phi_T L}{\Phi_S}\widehat{\widehat{S}}(z_1)\right]=0 \tag{17}$$

This equation is solved for S_b using known quantities pertaining to the flow and the ice. The fluxes q_{T*} and q_{S*} can subsequently be evaluated, with the following steps leading to q_{S*}:

$$W_b=\frac{u_*[\widehat{\widehat{S}}(z_1)-S_b]}{\Phi_S(S_b-S_{\text{ice}})} \tag{18}$$

$$q_{S*}=-W_b[S_{\text{ice}}-\widehat{\widehat{S}}(z_1)] \tag{19}$$

In all our simulations, $W_b \ll u_*$, which justifies the omission of the vertical motion of the top boundary over the time duration considered in this study, allowing us to simplify the approach by not coupling the LES model with a model for ice evolution. The boundary conditions for the scalars at the bottom of the domain are small outward temperature and salinity gradients of magnitude similar to the respective gradients inside the domain adjacent to the bottom boundary.

2.5. Initial Conditions

To set up the initial velocity, we consider a simple model of the oceanic boundary layer near the surface in which the momentum balance is between the Coriolis force and eddy-viscosity forces:

$$-fv=\nu_t\frac{\partial^2 u}{\partial z^2} \tag{20}$$

$$fu=\nu_t\frac{\partial^2 v}{\partial z^2} \tag{21}$$

with $u = U_b$ and $v = 0$ at $z = 0$ and $u,\ v \to 0$ as $z \to -\infty$. The solution is

$$u=U_b\ \exp(z/\delta)\cos(z/\delta) \tag{22}$$

$$v=U_b\ \exp(z/\delta)\sin(z/\delta) \tag{23}$$

where $\delta=\sqrt{2\nu_t/f}$. We assume a constant value $\nu_t=1.0\times10^{-3}$ m^2 s^{-1} and initialize our simulations with mean velocity profiles according to (22) and (23). A small amount of noise is also added. We use vertical profiles of temperature and salinity measured by an ITP in the ocean under sea ice in the Canada Basin for our initial temperature and salinity conditions. The in situ temperature and practical salinity from the ITP record are converted to potential temperature θ and absolute salinity S, respectively, using TEOS-10.

3. Results

For each initial vertical temperature profile, we perform 10 different LES experiments with ice-drift velocities U_b = 0.03, 0.06, 0.09, 0.12, 0.15, 0.18, 0.21, 0.24, 0.27, and 0.30 m s^{-1}. All the statistics presented in this section are time-averaged between 12 and 14 eddy turnover times, where an eddy turnover time is the ratio of the mixed layer depth z_m to the friction velocity u_*. The domain-averaged kinetic energy (not shown) in all simulations is very close to steady during that interval, with RMS fluctuations in a typical simulation approximately 3% of the mean, indicating that quasi-equilibrium has been reached. For the lowest to the largest ice-drift velocity, the 12–14th eddy turnover time averaging window corresponds, in physical time, to 129–151, 66–77, 46–53, 35–41, 27–32, 24–27, 21–25, 18–21, 16–18, and 14–17 h. All quantities shown in vertical profiles are horizontally averaged. Time averaging is denoted by an overbar, $(\overline{..})$, and horizontal averaging is denoted by angle brackets, $(\langle..\rangle)$.

3.1. PSW Only Versus PSW + NSTM

We investigate heat transfer from the ocean to the basal surface of drifting sea ice for two initial temperature profiles θ_0 in the Canada Basin. They are shown as the black lines in Figures 3a and 3b. The first profile (Figure 3a) will be referred to as "PSW only" and is representative of the early summer, having a uniform mixed layer temperature and a temperature peak corresponding to PSW just at the base of the mixed layer. The second profile (Figure 3b) will be referred to as "PSW + NSTM" and is typical of the late summer, featuring an NSTM within the mixed layer in addition to the PSW temperature peak just below the mixed layer.

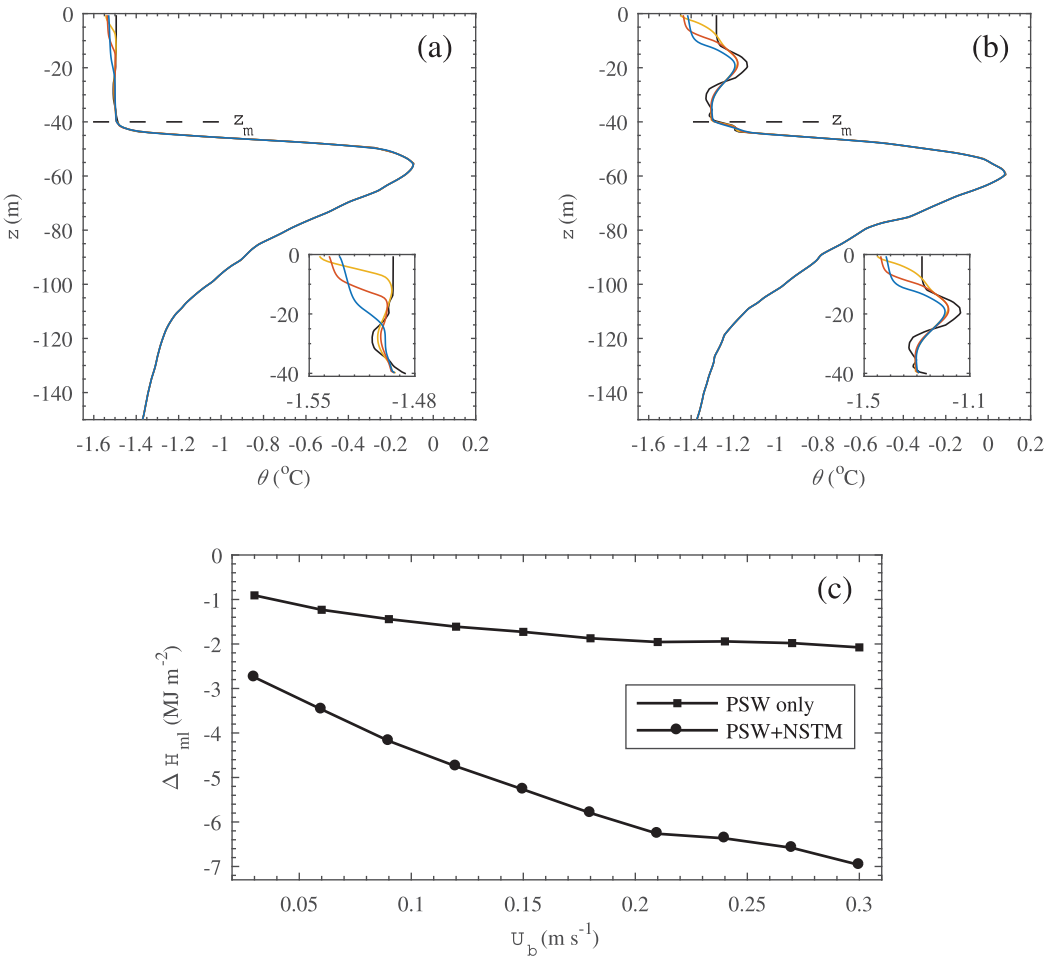

Figure 3. Initial temperature θ_0 (solid black line) and final temperature $\langle\bar{\theta}\rangle$ profiles from simulations with U_b=0.03 m s^{-1} (yellow line), 0.15 m s^{-1} (red line), and 0.30 m s^{-1} (blue line) for (a) "PSW only" case and (b) "PSW + NSTM" case. The mixed layer depth z_m is indicated by a horizontal dashed line. (c) Change in heat content ΔH_{ml} of the mixed layer for all U_b.

The two profiles were both collected by ITP 77. The "PSW only" one is from 14 June 2014 at the location 143.0°W and 73.6°N while the "PSW + NSTM" one is from 14 July 2014 at the location 150.5°W and 74.3°N. The corresponding vertical salinity profiles S_0 are shown in supporting information. The initial freezing temperature $\theta_b = -mS_b$ at the basal surface is −1.55°C in the "PSW only" case and −1.48°C in the "PSW + NSTM" case. The roughness length z_0 (Table 1) is based on field measurements at the site of ITP 77 on 14 June 2014 (Cole et al., 2017). While z_0 changes when ice melts (Ramudu et al., 2016), the effect of its variation is beyond the scope of this study. The ITP measurements start about 8–12 m underneath the basal ice surface. We extrapolate the temperature and salinity measurement at the first recorded depth level to the basal ice surface in our initial profiles. In both configurations, the mixed layer depth z_m is about 40 m.

In addition to the initial temperature profiles, we present the final temperature profiles $\langle\bar{\theta}\rangle$ from the simulations with the slowest-moving ice (U_b=0.03 m s^{-1}), ice moving at an intermediate velocity (U_b=0.15 m s^{-1}), and the fastest-moving ice (U_b=0.30 m s^{-1}) in Figures 3a and 3b. A thermal boundary layer exists at the ice-ocean interface because the temperature at the interface is at the freezing point θ_b and hence different from the temperature in the mixed layer. The thickness of the thermal boundary layer increases and the temperature difference across it decreases with increasing U_b due to the strength of the shear-driven mixing, which tends to homogenize the layer. These trends are more obvious in Figure 3a. In the "PSW + NSTM" case (Figure 3b), turbulence from the action of the drifting basal ice surface is responsible for the erosion of the NSTM layer. Heat from the NSTM layer is entrained upward and is also mixed downward, causing the temperature of the water immediately below the NSTM to increase. There is no temperature change in the PSW layer in our experiments.

We calculate the change in heat content of the mixed layer ΔH_{ml} in our simulations according to

$$\Delta H_{\mathrm{ml}} = \int_{z_m}^{0} \rho c_p [\langle \bar{\theta} \rangle (z) - \theta_0(z)] dz \tag{24}$$

The variation of ΔH_{ml} with U_b is shown in Figure 3c. In the "PSW + NSTM" case, the mixed layer initially contains more heat than in the "PSW only" case both because it features an NSTM and because it is at a higher temperature. Over the course of the same integration period, the "PSW + NSTM" case thus loses more heat than the "PSW only" case at all U_b due to enhanced turbulent entrainment.

Figure 4a shows the velocity components $\langle \bar{u} \rangle$ and $\langle \bar{v} \rangle$ from our simulations for both the "PSW only" and "PSW + NSTM" cases for $U_b = 0.15$ m s^{-1}, an intermediate value in the range of ice-drift velocities we consider. The velocity profiles in the mixed layer represent an Ekman spiral. Cole et al. (2014) also reported Ekman veering under sea ice drifting under the action of the wind using ocean velocity observations from the Canada Basin. In the "PSW only" case, the velocity maxima are located at a greater depth than in the "PSW + NSTM" case. This occurs because the mixed layer is characterized by a small salt stratification below about 15 m in the presence of the NSTM (see supporting information). This salt stratification tends to keep the mixed layer stable, opposing the destabilizing effect of the surface shear stress and thus limiting the depth at which the velocity peaks in the "PSW + NSTM" case.

The friction velocity $\langle \overline{u_*} \rangle$ in all the simulations for both "PSW only" and "PSW + NSTM," presented in Figure 4b, increases almost linearly with U_b. It is also independent of the vertical temperature or salinity structure in the mixed layer.

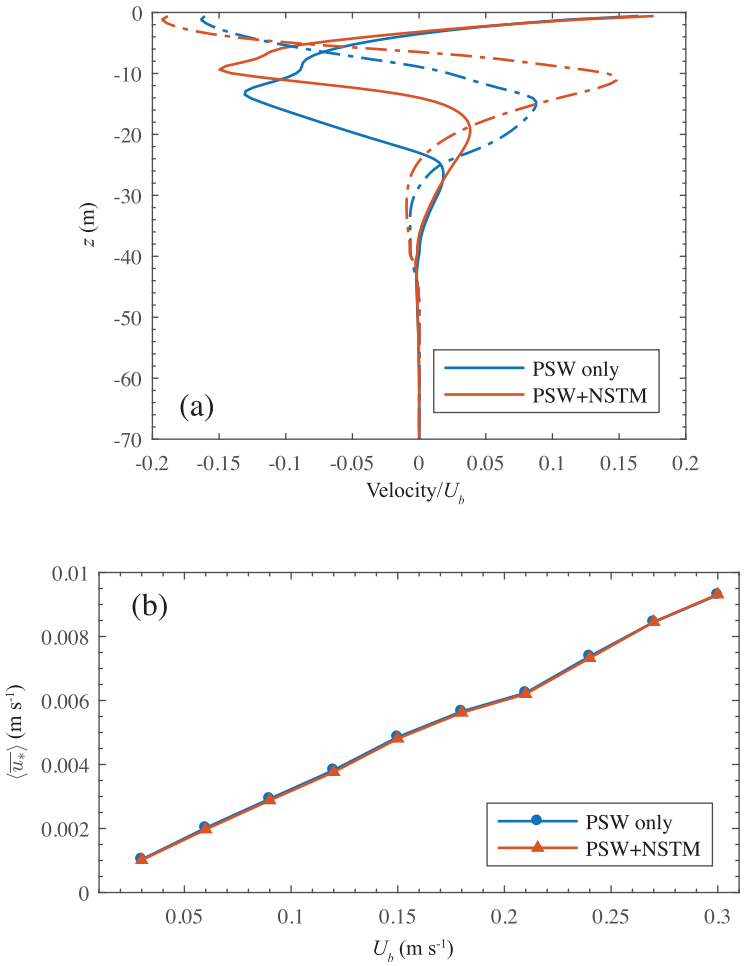

Figure 4. (a) Normalized horizontal velocity components $\langle \bar{u} \rangle$ (solid line) and $\langle \bar{v} \rangle$ (dash-dot line) from the simulation with $U_b = 0.15$ m s^{-1}. The points $\langle \bar{u} \rangle / U_b = 1$ and $\langle \bar{v} \rangle / U_b = 0$ at $z = 0$ are omitted. (b) Friction velocity $\langle \overline{u_*} \rangle$ for all U_b.

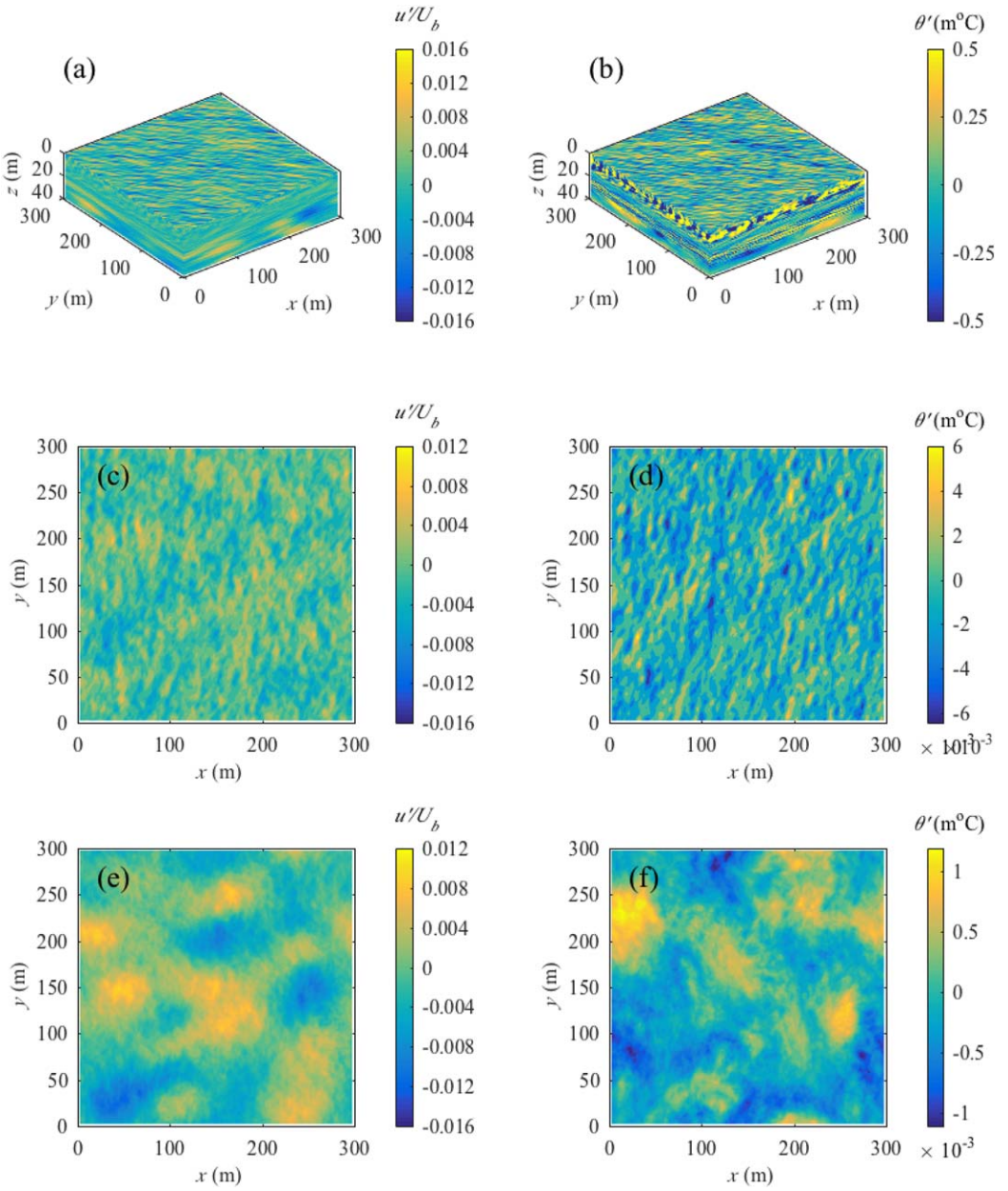

Figure 5. Three-dimensional contour plots of (a) u'/U_b and (b) θ'. Horizontal cross sections at $z=-4.1$ m of (c) u'/U_b and (d) θ'. Horizontal cross sections at $z=-35.2$ m of (e) u'/U_b and (f) θ'.

We also investigate the spatial fluctuations u' and θ' within the top 40 m for the "PSW + NSTM" case with $U_b=0.15$ m s^{-1}. u' and θ' are defined as $u'=\bar{u}-\langle\bar{u}\rangle$ and $\theta'=\bar{\theta}-\langle\bar{\theta}\rangle$. The three-dimensional contour plots of Figures 5a and 5b indicate that the turbulent field at the surface consists of streaks deflected to the right of the ice-drift velocity U_b. The horizontal cross sections at a depth $z=-4.1$ m are shown in Figures 5c and 5d and the horizontal cross sections at a depth $z=-35.2$ m (near the base of the mixed layer) are shown in Figures 5e and 5f. It can be seen that the length scale characterizing the turbulence is smaller at the surface than at the base of the mixed layer. At the surface, the turbulence is caused by the applied shear stress while at the base of the mixed layer, it is caused by internal waves. These two physical processes impose different length scales on the turbulence field. The ability of LES to resolve these different features and length scales makes it a valuable tool to use for this study. There are no major differences in the turbulent length scales between the "PSW + NSTM" case and "PSW only" case.

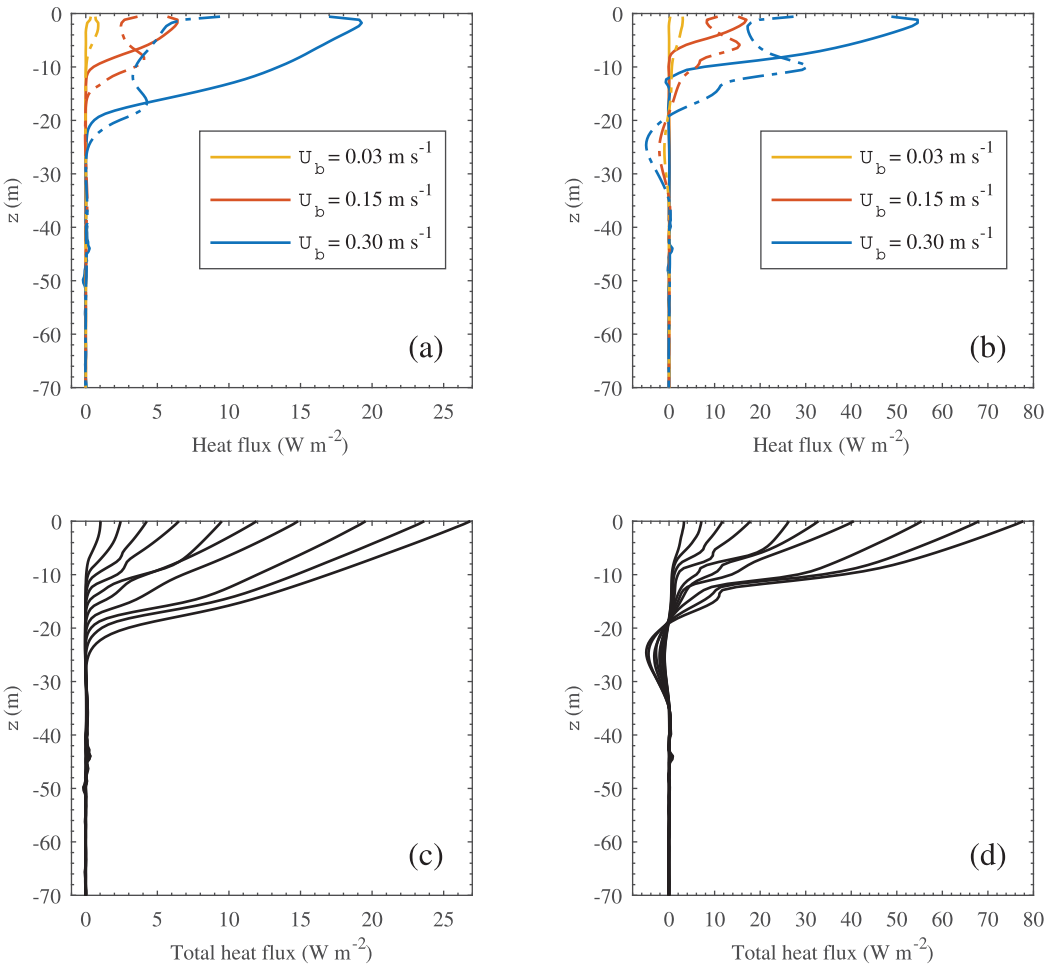

Figure 6. Resolved heat flux $\rho_0 c_\ell \langle \overline{w'\theta'} \rangle$ (solid lines) and SGS heat flux $\rho_0 c_\ell \langle \overline{K_T \partial\theta/\partial z} \rangle$ (dash-dotted lines) for the (a) "PSW only" case and (b) "PSW + NSTM" case. Total vertical heat flux (resolved + SGS) for the (c) "PSW only" case and (b) "PSW + NSTM" case. In Figures 6c and 6d, the profiles from left to right correspond to U_b increasing monotonically from 0.03 to 0.30 m s^{-1}.

Figures 6a and 6b present the resolved heat flux $\rho_0 c_\ell \langle \overline{w'\theta'} \rangle$ (in W m^{-2}) and SGS heat flux $\rho_0 c_\ell \langle \overline{K_T \partial\theta/\partial z} \rangle$ (in W m^{-2}) for the "PSW only" and "PSW + NSTM" cases, respectively, for U_b= 0.03, 0.15, and 0.30 m s^{-1}. $\overline{w'\theta'}$ is defined as $\overline{w'\theta'} = \overline{w\theta} - \bar{w}\bar{\theta}$ and positive values indicate warm water moving upward. These two figures show that at higher ice-drift velocities, the SGS component is smaller than the resolved component, indicating that the LES can resolve a large fraction of the turbulence. At the lowest U_b, although the shear stress at the surface is small, there is still turbulent convective motion near the ice-ocean interface due to buoyancy differences. This motion is captured by the SGS model to give nonzero eddy thermal diffusivities, which consequently leads to nonzero SGS vertical heat fluxes near the surface. The total vertical heat flux (resolved + SGS) for all U_b is plotted in Figures 6c and 6d for "PSW only" and "PSW + NSTM," respectively. No heat is entrained from the PSW layer even at the largest U_b, so that the temperature of the PSW layer stays unchanged. The output from our simulations therefore support the result of Toole et al. (2010), who did not explicitly resolve the turbulent heat flux, that the heat trapped in the PSW layer is shielded from the basal ice surface by the strong salinity stratification at the base of the mixed layer. Heat is entrained only from within the mixed layer as a result of the shear stress-induced turbulence by drifting sea ice. The heat flux $Q_{T*} = \rho_0 c_\ell q_{T*}$ at the basal ice surface increases monotonically with U_b and the presence of the NSTM amplifies the heat entrained to the basal ice surface roughly by a factor of 3. In the "PSW + NSTM" case, we also note the negative (downward) heat flux at the bottom end of the NSTM layer due to the turbulence mixing heat from the NSTM layer downward.

The basal ice roughness length $z_0 = 1.2 \times 10^{-5}$ m chosen in this study is on the lower end of the range of roughness lengths typically observed in the Arctic (Cole et al., 2017). Additional simulations of the "PSW + NSTM" case (not shown) were run with larger values of z_0 at a fixed $U_b = 0.15$ m s^{-1} for a sensitivity study of how the basal surface heat flux Q_{T*} changes with roughness z_0. It was found that when z_0 increases by 2 orders of magnitude, Q_{T*} increases by a factor of 2 approximately. Still no heat was entrained from the PSW layer at the largest z_0 considered. Details of this study will be reported in future work.

Gallaher et al. (2016) reported measurements of the friction velocity u_* and vertical heat flux collected by the Naval Postgraduate School Autonomous Ocean Flux Buoy (AOFB) 33 (www.oc.nps.edu/~stanton/fluxbuoy), deployed on the same ice floe as ITP 77. AOFB 33 samples at a depth of 4.5 m or initially 2 m below the basal ice surface. Although the setup of our LES experiments is idealized, the outputs of friction velocity and total heat flux generally fall within the range of field measurements. The turbulent heat flux is observed to become larger when the NSTM starts developing in the mixed layer, consistent with the results of our simulations.

3.2. Modified NSTM

The magnitude of the temperature anomaly of the NSTM that develops within the mixed layer in the Canada Basin is variable. The NSTM evolves over time since it is a seasonal feature and also changes spatially since it depends on incoming solar radiation and the distribution of open water areas. Observations between 2002 and 2007 show that the NSTM is warmest south of 75°N and near the coast but that north of 75°N, the temperature peak of the NSTM has been steadily increasing (Jackson et al., 2010). Some vertical temperature profiles collected by ITPs recently show that the temperature peak corresponding to the NSTM can be as large as the temperature peak corresponding to the PSW layer itself. Gallaher et al. (2016) observed that turbulent heat fluxes often exceeded 100 W m^{-2} when the ocean mixed layer heat content, and hence the size of the NSTM, is large, contributing to well above-average basal ice melt rates. Given the impact of the NSTM on sea ice melt rates, it is important to understand the relationship between the heat content of the NSTM and turbulent heat delivery to the basal surface of sea ice.

To study this relationship, we repeat the LES experiments of section 3.1 for five new cases, each with a different initial NSTM size (Figure 7a). The new initial temperature profiles are obtained by artificially modifying the temperature in the NSTM layer, which occupies the depths 11–26 m, in the "PSW + NSTM" case from section 3.1. The original "PSW + NSTM" profile is referred to as "NSTM 1." The temperature at all other depths outside the original NSTM layer is unmodified. In "NSTM 6," the maximum temperature of the NSTM is equal in magnitude to the PSW maximum temperature. The initial heat content of the NSTM layer increases linearly from "NSTM 1" to "NSTM 6."

Simulation results for the heat flux Q_{T*} at the basal ice surface are plotted in Figure 7b for "NSTM 1" to "NSTM 6." For comparison, Q_{T*} for the "PSW only" case of section 3.1 is also included. Q_{T*} increases monotonically in magnitude with U_b and the size of the NSTM. We can define a scaling law relating Q_{T*} to U_b and $\Delta\theta$, $\Delta\theta$ being the difference between the initial mean temperature of the mixed layer ($0 \le z \le z_m$) and the initial in situ freezing temperature $\theta_b = -mS_b$ at the surface. The effect of changing the roughness length z_0 is not included in this scaling law. Figure 8a shows the fit of the dimensionless groups $a(c_\ell \Delta\theta / U_b^2)^{b_1} (U_b/(z_m f))^{b_2}$ to $Q_{T*}/\rho_0 c_\ell U_b \Delta\theta$, where a, b_1, and b_2 are fit coefficients evaluated to be $a = 1.47$, $b_1 = -0.62$, and $b_2 = -0.74$. We thus propose for Q_{T*} the scaling law

$$Q_{T*} = 1.47 \left(\frac{c_\ell \Delta\theta}{U_b^2}\right)^{-0.62} \left(\frac{U_b}{z_m f}\right)^{-0.74} \rho_0 c_\ell U_b \Delta\theta \tag{25}$$

Q_{T*} varies with $U_b^{1.50}$ and $\Delta\theta^{0.38}$. The dependence on $\Delta\theta$ is sublinear because melting is a negative feedback process: melting results in the development of stratification at the ice-ocean interface, which suppresses heat delivery to the basal ice surface and hence further melting. The comparison between Q_{T*} from (25) and from the LES experiments is presented in a log-log plot in Figure 8b, with a black 1:1 line included. While there is good agreement between the two sets of Q_{T*}, the slight departures from the 1:1 line especially at the low and high ends of the range possibly indicate that different physical scales should be used for the scaling law for different ranges of Q_T*.

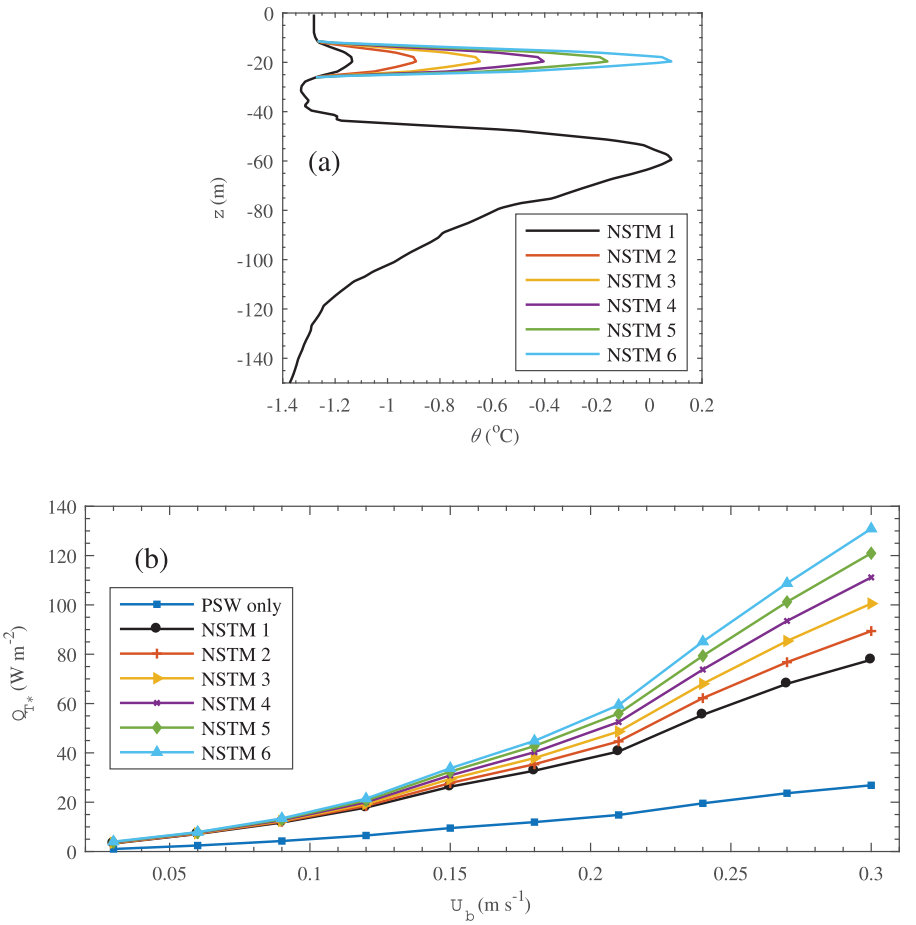

Figure 7. (a) Initial temperature profiles for cases "NSTM 1" to "NSTM 6." (b) Basal surface heat flux Q_{T*} for "NSTM 1" to "NSTM 6" and all U_b.

The "PSW only" and "NSTM 1" to "NSTM 6" profiles are comparable to vertical temperature profiles commonly observed across the Canada Basin. There may be differences between actual observations and the profiles considered in our experiments in terms of the depth of the NSTM, depth of the PSW, and stratification strength. Nevertheless, the scaling law in (25) can be used to obtain an inexpensive estimate of the heat flux to the basal ice surface due to turbulent entrainment from the mixed layer and its subsequent contribution to basal melting in models of sea ice evolution in the Arctic.

McPhee et al. (1999) proposed a simpler expression for the heat flux at the basal ice surface and we will refer to the heat flux from this expression as Q^{M}_{T*}:

$$Q^{\mathrm{M}}_{T*} = c_H \rho_0 c_\ell u_* \Delta\theta \tag{26}$$

$c_H = 0.006$ is a heat transfer coefficient. Our parameterization (25) can be rewritten as:

$$Q_{T*} = (1.47\, c_\ell^{-0.62} z_m^{0.74} f^{0.74})\, \rho_0 c_\ell U_b^{1.50} \Delta\theta^{0.38} \tag{27}$$

and the results shown in Figure 4b suggest the relationship $u_* \approx 0.032\, U_b$ in our simulations. Substituting this into (27) and further simplifying yields

$$Q_{T*} = C \rho_0 c_\ell u_*^{1.50} \Delta\theta^{0.38} \tag{28}$$

with $C = 0.033\,\mathrm{m}^{-0.50}\mathrm{s}^{0.50}\mathrm{K}^{-0.62}$. Figure 9 shows the percentage difference between Q_{T*} from (28) and Q^{M}_{T*} from (26) for $\Delta\theta$ from the profiles "NSTM 1" to "NSTM 6" and for u_* corresponding to all U_b. The basal heat fluxes from the two expressions are of the same order. We attribute the differences between them to (28) having a super-linear dependence on u_* and sublinear dependence on $\Delta\theta$.

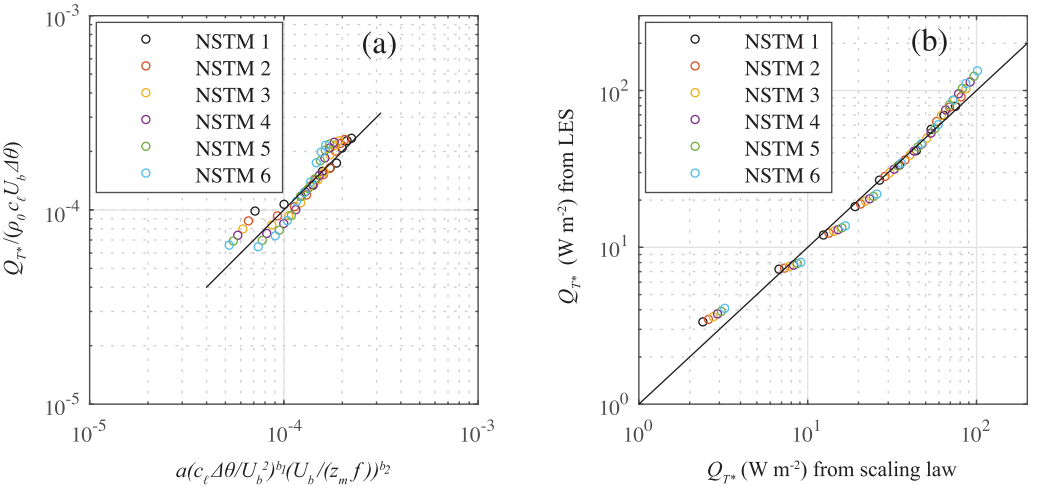

Figure 8. (a) Fit of $a(c_\ell \Delta\theta/U_b^2)^{b_1}(U_b/(z_m f))^{b_2}$ to $Q_{T*}/\rho_0 c_\ell U_b \Delta\theta$. (b) Comparison of Q_{T*} from LES with Q_{T*} from (25).

4. Case Study: Turbulent Heat Entrainment During "The Great Arctic Cyclone of 2012"

A large cyclone, commonly referred to as "The Great Arctic Cyclone of 2012," passed over the Arctic in early August 2012. It lasted almost 13 days and its pressure minimum was the lowest recorded for August cyclones since 1979. Arctic sea ice extent was going to reach a record low after summer 2012, but the passage of the cyclone caused that record low to be reached a few weeks earlier than predicted (Simmonds & Rudeva, 2012).

Zhang et al. (2013) used the Pan-arctic Ice-Ocean Modeling and Assimilation System (PIOMAS) to model the effect of the cyclone on the sea ice pack. The cyclone moved over the ice-covered areas of the Pacific sector (ICAPS) of the Arctic on 6–8 August. The ICAPS is defined to be between 90°E and 90°W in the Arctic and covers an area of 3.87×10^6 km^2 based on satellite observations. The rate of sea ice melt in the ICAPS increased to 0.17×10^3 km^3 d^{-1} during the 3 day period of 6–8 August from 0.08×10^3 km^3 d^{-1} during the 3 day period of 2–4 August just before the arrival of the cyclone. Melting at the bottom by ocean dynamic heat transport was the main mechanism contributing to the increase in total melt rate, accounting for 0.10×10^3 km^3 d^{-1} during the cyclone as opposed to only 0.02×10^3 km^3 d^{-1} before. Bottom melt increased because the cyclone caused enhanced heat entrainment from the NSTM. Using (11) with the second term on the right neglected, we estimate the average basal ice surface heat flux over the ICAPS responsible for the 0.10×10^3 km^3 d^{-1} of cyclone-associated bottom melting to be 83 W m^{-2}.

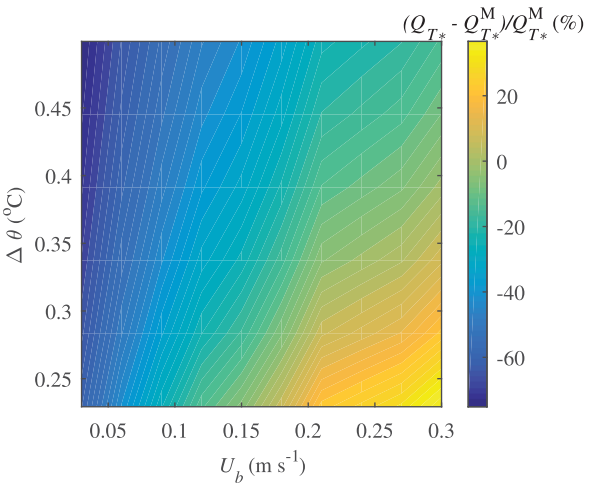

Figure 9. Percentage difference between Q_{T*} from (28) and Q_{T*}^M from (26) for $\Delta\theta$ from "NSTM 1" to "NSTM 6" and u_* corresponding to all U_b.

A case study of "The Great Arctic Cyclone of 2012" is conducted using LES. The physical domain size is the same as in previous experiments and all the constants used are the same as in Table 1. U_b is taken to be 0.18 m s^{-1}, equivalent to the average ice-drift speed during the cyclone simulated by Zhang et al. (2013). The initial temperature profile, shown in Figure 10a, and initial salinity profile, shown in the supporting information, are from ITP 41 collected on 3 August 2012 at longitude 137.8°W and latitude 74.5°N. The surface heat flux Q_{T*} output by the simulation is 57 W m^{-2} (Figure 10b). Using a mixed layer depth of 45 m, the scaling law from (25) yields $Q_T* = 62$ W m^{-2}. This indicates that the upward heat flux entrained from the heat stored in the ocean by the shear-induced turbulence alone was responsible for roughly 70% of the total ocean-to-ice heat flux during this event.

5. Summary

The Arctic Ocean has been losing sea ice due to increased melting since the 1980s, and this decline in sea ice has been particularly

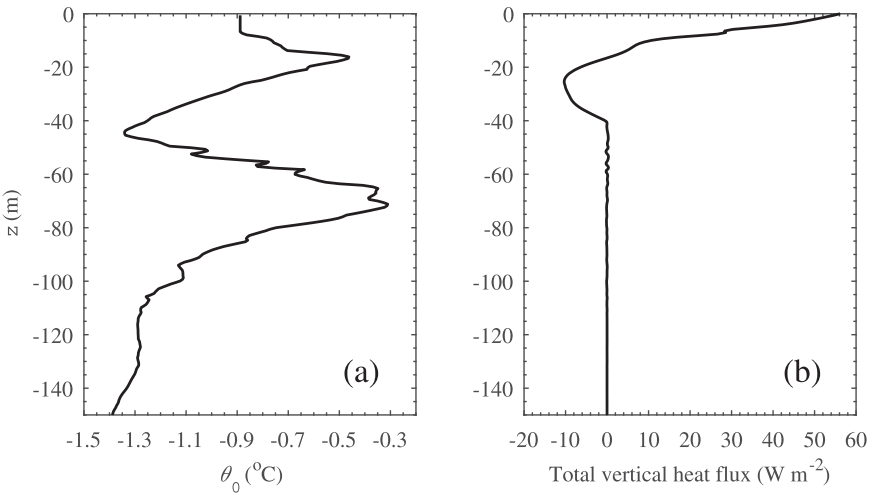

Figure 10. (a) Initial temperature profile from ITP 41 on 3 August 2012. (b) Total heat flux from LES.

pronounced in the Canada Basin. Warm PSW sits at the base of the mixed layer in the Canada Basin and during the summer, the NSTM develops near the surface, storing solar radiation as heat within the mixed layer. It is thought that the presence of the PSW and NSTM water masses has contributed to the observed accelerated melting of sea ice, but the interaction of these two anomalously warm layers with the basal surface of sea ice is not fully known. In order to understand this process better, we use an LES model to study heat transport in a rectangular domain occupying the upper 150 m of the ocean as ice drifts over the surface. LES enables us to resolve the turbulent entrainment of heat not captured explicitly by climate models.

A comparison between the case where the upper ocean features a PSW layer only and the case where it features both the PSW and NSTM layers revealed that in the presence of the NSTM, the heat flux to the basal ice surface is about 3 times larger. Our modeled heat flux near the surface agrees generally well with field observations. There is almost no heat entrained from the PSW layer over the range of ice-drift velocities considered. This leads to the conclusion that the stratification barrier at the base of the mixed layer is too strong to allow heat from the PSW layer to escape upward. Since the NSTM itself varies spatially and temporally in the Arctic, we additionally study cases with NSTM sizes larger than in the original case. A scaling law for the basal heat flux is proposed based on the ice-drift velocity and the difference between the initial mean temperature of the mixed layer and the initial freezing temperature at the surface.

Using our LES model, a case study of the effect of "The Great Arctic Cyclone of 2012" yields a basal surface heat flux of 57 W m^{-2} during the passage of the cyclone. This is compared with the 83 W m^{-2} that we estimated from the PIOMAS-based study of Zhang et al. (2013) was responsible for the enhanced bottom melting during the cyclone. The results from our idealized LES setup indicates that a significant fraction (70%) of the total basal heat flux that caused bottom melting was purely due to the action of the drifting ice entraining heat upward from the mixed layer. In order to simulate this effect, large-scale climate models must be able to account for the NSTM layer. This may require a careful treatment of the optics of the NSTM layer (Kim et al., 2016) in addition to entrainment of heat to the surface. Given the coarse resolution (order of ~10 m vertically) of many climate models, it is far from clear that these processes are currently accurately resolved.

It is thus important to investigate how results from the LES model used in this study compare against results from ocean general circulation models using different mixed layer parameterizations. Furthermore, while almost no heat entrainment from the PSW was found, the PSW still represents a significant reservoir of heat sitting dangerously close to sea ice in the Arctic. Would a less strongly stratified pycnocline allow heat entrainment from the PSW more easily? Given the increased melting of sea ice, leads are becoming prominent in the ice cover especially in the summer. What is the impact of leads on ocean-to-ice heat transfer? These questions will be addressed in further research.

Appendix A: LES Model Testing and Validation

We perform the simulation of McWilliams et al. (1997) for shear turbulence in the planetary boundary layer (PBL) of the ocean to test and validate our LES code, in particular its solution for scalars. This simulation includes the effect of temperature but not salinity. While our study of the flow under Arctic sea ice involves both temperature and salinity, it is sufficient to test the code with a case that involves only temperature, because the same advection-diffusion equation is used to solve for the evolution of salinity in our simulations.

We solve (1), (2), and (3) in a three-dimensional rectangular domain with the top corresponding to the ocean surface; ρ in (1) is here evaluated using a linear equation of state, $\rho=\rho_0(1-\alpha\theta)$, where $\alpha=2\times10^{-4}{}^{\circ}\mathrm{C}^{-1}$ is the thermal expansion coefficient of seawater. A shear stress $\tau=0.037$ N m^{-2}, equivalent to $u_*=6.1\times10^{-3}$ m s^{-1} is applied at the top of the domain in the x-direction and a heat flux $q_{T*}=-5$ W m^{-2} leaves the top surface. Although these momentum and heat flux boundary conditions are constants and hence simpler than in our application, they serve our objective of validating our coupled momentum and scalar solver. The effect of the shear stress on the turbulence and the mean flow is much stronger than the effect of surface cooling.

The domain length is $L_x=L_y=150$ m and $L_z=90$ m. The domain consists of a mixed layer of depth z_m and a layer stably stratified by temperature underneath. The simulation is set up such that z_m is initially 33 m, with the temperature θ_0 homogeneous from the surface to z_m and decreasing with depth by $\partial\theta_0/\partial z=0.01$ K m^{-1} below z_m. The computational grid size is $N_x=N_y=50$ and $N_z=150$. The simulation is run until it reaches a quasi-equilibrium state and we take statistics over a length of time during this quasi-equilibrium state. Yang et al. (2015) performed a similar LES validation exercise, although they considered the additional effect of Stokes drift giving rise to Langmuir turbulence and reported only statistics related to the velocity field.

Figure A1 shows the comparison of the horizontally averaged and time-averaged velocity components $\langle\bar{u}\rangle$ and $\langle\bar{v}\rangle$, total vertical heat flux, and temperature variance $\langle\overline{\theta'^2}\rangle$ from our simulation against those of McWilliams et al. (1997). $\overline{\theta'^2}$ is evaluated as $\overline{\theta'^2}=\overline{\theta\theta}-\bar{\theta}\bar{\theta}$. The two sets of profiles of velocity components match each other very closely. The heat flux and temperature profiles agree reasonably well also. We attribute the difference between them to the eddy-viscosity model in our simulation being different from that of McWilliams et al. (1997). Nieuwstadt et al. (1993) showed that different eddy-viscosity parameterizations give horizontally averaged heat flux and temperature variance profiles that are slightly different from each other in their LES of the atmospheric boundary layer.

Appendix B: Variable Quantities

The list of variable quantities in this study and the symbols used to denote them is given in Table B1.

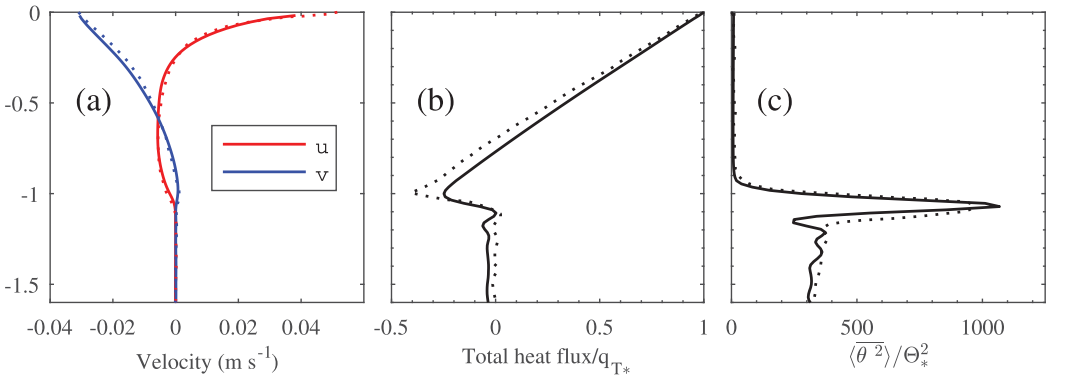

Figure A1. (a) Velocity components $\langle\bar{u}\rangle$ and $\langle\bar{v}\rangle$, (b) total vertical heat flux ($\langle\overline{w'\theta'}\rangle+\langle\overline{K_T\partial\theta/\partial z}\rangle$) normalized by q_{T*}, and (c) temperature variance $\langle\overline{\theta'^2}\rangle$ normalized by Θ_*^2, where $\Theta_*=q_{T*}/u_*$. Solid lines: our simulation, dotted lines: McWilliams et al. (1997).

Table B1
Variables Used

Quantity	Symbol	Units
Fit coefficients in scaling law	a, b_1, b_2	
Heat transfer coefficient	c_H	
Dimensional constant in heat flux parameterization	C	$m^{-0.50}s^{0.50}K^{-0.62}$
Smagorinsky coefficient	C_s	
Heat content of mixed layer	H_{ml}	$J\ m^{-2}$
Indices denoting direction	i, j	
Molecular salt diffusivity	k_S	$m^2\ s^{-1}$
Molecular thermal diffusivity	k_T	$m^2\ s^{-1}$
Subgrid-scale salt eddy diffusivity	K_S	$m^2\ s^{-1}$
Subgrid-scale thermal eddy diffusivity	K_T	$m^2\ s^{-1}$
Length of domain	L_x, L_y, L_z	m
Number of computational grid points	N_x, N_y, N_z	
Kinematic pressure	p	$m^2\ s^{-2}$
Turbulent subgrid-scale Prandtl number	Pr_{SGS}	
Heat flux through ice	q_{ice}	$K\ m\ s^{-1}$
Subgrid-scale salt flux	$q_{S,i}$	$g\ kg^{-1}\ m\ s^{-1}$
Salt flux at ice-ocean interface (at $z = 0$)	q_{S*}	$g\ kg^{-1}\ m\ s^{-1}$
Subgrid-scale heat flux	$q_{T,i}$	$K\ m\ s^{-1}$
Heat flux at ice-ocean interface (at $z = 0$)	q_{T*}	$K\ m\ s^{-1}$
Heat flux at ice-ocean interface (at $z = 0$)	Q_{T*}	$W\ m^{-2}$
Initial salinity	S_0	$g\ kg^{-1}$
Salinity of ocean water at ice-ocean interface (at $z = 0$)	S_b	$g\ kg^{-1}$
Strain rate	$\mathcal{S}_{i,j}$	s^{-1}
Turbulent subgrid-scale Schmidt number	Sc_{SGS}	
Time	t	s
Velocity along x and y directions respectively	u, v	$m\ s^{-1}$
Friction velocity	u_*	$m\ s^{-1}$
Velocity vector	u_i	$m\ s^{-1}$
Relative velocity	$u_{r,i}$	$m\ s^{-1}$
Velocity of ocean water at ice-ocean interface (at $z = 0$)	U_b	$m\ s^{-1}$
Vertical velocity of ice-ocean interface	W_b	$m\ s^{-1}$
Displacement vector components	x, y, z	m
Displacement (distance and direction) vector	x_i	m
Vertical distance of first grid point from ice-ocean interface	z_1	m
Mixed layer depth	z_m	m
Ekman layer depth	δ	m
Grid cutoff filter size in LES	Δ	m
Grid size	$\Delta_x, \Delta_y, \Delta_z$	m
Potential temperature	θ	°C
Initial temperature	θ_0	°C
Freezing temperature at ice-ocean interface (at z=0)	θ_b	°C
Salinity-dependent and pressure-dependent freezing point at a depth z	θ_f	°C
Friction temperature	Θ_*	°C
Molecular viscosity	ν	$m^2\ s^{-1}$
Eddy viscosity	ν_t	$m^2\ s^{-1}$
Potential density	ρ	$kg\ m^{-3}$
Subgrid-scale shear stress	$\tau_{i,j}$	$m^2\ s^{-2}$
Parameters in Monin-Obukhov similarity theory	Φ_T, Φ_S	

Acknowledgments
The Ice-Tethered Profiler data were collected and made available by the Ice-Tethered Profiler Program (Krishfield et al., 2008; Toole et al., 2010) based at the Woods Hole Oceanographic Institution (http://www.whoi.edu/itp). We thank Thomas Haine and Xiang I. A. Yang for helpful discussion. ER, RG, and AG are financially supported by NOAA grant NA15OAR4310172. DY acknowledges support from his start-up fund at the University of Houston and CM is partially supported by NSF. Supporting information is being provided on the Harvard Dataverse repository (Ramudu et al., 2017) to enable the figures to be reproduced and the full data set is available by contacting the corresponding author at gnanades@jhu.edu.

References

Albertson, J. D., & Parlange, M. B. (1999). Surface length scales and shear stress: Implications for land-atmosphere interaction over complex terrain. *Water Resources Research*, *35*(7), 2121–2132. https://doi.org/10.1029/1999WR900094

Antonopoulos-Domis, M. (1981). Large-eddy simulation of a passive scalar in isotropic turbulence. *Journal of Fluid Mechanics*, *104*, 55–79. https://doi.org/10.1017/S0022112081002814

Bou-Zeid, E., Meneveau, C., & Parlange, M. (2005). A scale-dependent Lagrangian dynamic model for large eddy simulation of complex turbulent flows. *Physics of Fluids*, *17*(2), 025105. https://doi.org/10.1063/1.1839152

Calaf, M., Parlange, M. B., & Meneveau, C. (2011). Large eddy simulation study of scalar transport in fully developed wind-turbine array boundary layers. *Physics of Fluids*, *23*(12), 126603. https://doi.org/10.1063/1.3663376

Canuto, C., Hussaini, M., Quarteroni, Y. A., & Zang, T. A. (1988). *Spectral methods in fluid dynamics*. New York, NY: Springer.

Coachman, L. K., & Barnes, C. A. (1961). The contribution of Bering Sea water to the Arctic Ocean. *Arctic*, *14*(3), 147–161.
Cole, S. T., Timmermans, M.-L., Toole, J. M., Krishfield, R. A., & Thwaites, F. T. (2014). Ekman veering, internal waves, and turbulence observed under Arctic sea ice. *Journal of Physical Oceanography*, *44*(5), 1306–1328. https://doi.org/10.1175/JPO-D-12-0191.1
Cole, S. T., Toole, J. M., Lele, R., Timmermans, M.-L., Gallaher, S. G., Stanton, T. P., . . . Haas, C. (2017). Ice and ocean velocity in the Arctic marginal ice zone: Ice roughness and momentum transfer. *Elementa Science of the Anthropocene*, *5*, 55. https://doi.org/10.1525/elementa.241
Gallaher, S. G., Stanton, T. P., Shaw, W. J., Cole, S. T., Toole, J. M., Wilkinson, J. P., . . . Hwang, B. (2016). Evolution of a Canada Basin ice-ocean boundary layer and mixed layer across a developing thermodynamically forced marginal ice zone. *Journal of Geophysical Research: Oceans*, *121*, 6223–6250. https://doi.org/10.1002/2016JC011778
IOC, SCOR, and IAPSO (2010). *The international thermodynamic equation of seawater—2010: Calculation and use of thermodynamic properties* (English) (Manuals and Guides No. 56, 196 pp.). Paris, France: Intergovernmental Oceanographic Commission, UNESCO.
Jackson, J. M., Carmack, E. C., McLaughlin, F. A., Allen, S. E., & Ingram, R. G. (2010). Identification, characterization, and change of the near-surface temperature maximum in the Canada Basin, 1993–2008. *Journal of Geophysical Research*, *115*, C05021. https://doi.org/10.1029/2009JC005265
Johannessen, O. M., Shalina, E. V., & Miles, M. W. (1999). Satellite evidence for an Arctic sea ice cover in transformation. *Science*, *286*(5446), 1937–1939. https://doi.org/10.1126/science.286.5446.1937
Kantha, L. H., & Clayson, C. A. (2000). *Numerical models of oceans and oceanic processes*, *International Geophysical Services* (Vol. 66). San Diego, CA: Academic Press.
Kim, G. E., Gnanadesikan, A., & Pradal, M.-A. (2016). Increased surface ocean heating by colored detrital matter (CDM) linked to greater northern hemisphere ice formation in the GFDL CM2Mc ESM. *Journal of Climate*, *29*(24), 9063–9076. https://doi.org/10.1175/JCLI-D-16-0053.1
Kirchmeier-Young, M. C., Zwiers, F. W., & Gillett, N. P. (2017). Attribution of extreme events in Arctic sea ice extent. *Journal of Climate*, *30*(2), 553–571. https://doi.org/10.1175/JCLI-D-16-0412.1
Krishfield, R., Toole, J., Proshutinsky, A., & Timmermans, M.-L. (2008). Automated Ice-Tethered Profilers for seawater observations under pack ice in all seasons. *Journal of Atmospheric and Oceanic Technology*, *25*(11), 2091–2105. https://doi.org/10.1175/2008JTECHO587.1
Kumar, V., Kleissl, J., Meneveau, C., & Parlange, M. B. (2006). Large-eddy simulation of a diurnal cycle of the atmospheric boundary layer: Atmospheric stability and scaling issues. *Water Resources Research*, *42*, W06D09. https://doi.org/10.1029/2005WR004651
Kwok, R., & Rothrock, D. A. (2009). Decline in Arctic sea ice thickness from submarine and ICESat records: 1958–2008. *Geophysical Research Letters*, *36*, L15501. https://doi.org/10.1029/2009GL039035
Mason, P. J. (1989). Large-eddy simulation of the convective atmospheric boundary layer. *Journal of Atmospheric Sciences*, *46*(11), 1492–1516.
McPhee, M. (2008). *Air-ice-ocean interaction: Turbulent ocean boundary layer exchange processes*. New York, NY: Springer.
McPhee, M. G., Kottmeier, C., & Morison, J. H. (1999). Ocean heat flux in the Central Weddell Sea during winter. *Journal of Physical Oceanography*, *29*(6), 1166–1179. https://doi.org/10.1175/1520-0485(1999)029<1166:OHFITC>2.0.CO;2
McPhee, M. G., Maykut, G. A., & Morison, J. H. (1987). Dynamics and thermodynamics of the ice/upper ocean system in the marginal ice zone of the Greenland Sea. *Journal of Geophysical Research*, *92*(C7), 7017–7031. https://doi.org/10.1029/JC092iC07p07017
McPhee, M. G., Stanton, T. P., Morison, J. H., & Martinson, D. G. (1998). Freshening of the upper ocean in the Arctic: Is perennial sea ice disappearing? *Geophysical Research Letters*, *25*(10), 1729–1732. https://doi.org/10.1029/98GL00933
McWilliams, J. C., Sullivan, P. P., & Moeng, C.-H. (1997). Langmuir turbulence in the ocean. *Journal of Fluid Mechanics*, *334*, 1–30. https://doi.org/10.1017/S0022112096004375
Meier, W. N. (2017). Losing Arctic sea ice: Observations of the recent decline and the long-term context. In D. N. Thomas (Ed.), *Sea ice* (3 ed., Chap. 11, pp. 290–303). Chichester, UK: John Wiley & Sons.
Meneveau, C., Lund, T. S., & Cabot, W. H. (1996). A Lagrangian dynamic subgrid-scale model of turbulence. *Journal of Fluid Mechanics*, *319*, 353–385. https://doi.org/10.1017/S0022112096007379
Nieuwstadt, F. T. M., Mason, P. J., Moeng, C.-H., & Schumann, U. (1993). Large-eddy simulation of the convective boundary layer: A comparison of four computer codes. In F. Durst et al. (Eds.), *Turbulent shear flows 8: Selected papers from the eighth international symposium on turbulent shear flows* (pp. 343–367). Berlin, Germany: Springer.
Notz, D., & Stroeve, J. (2016). Observed Arctic sea-ice loss directly follows anthropogenic CO_2 emission. *Science*, *354*(6313), 747–750. https://doi.org/10.1126/science.aag2345
Orszag, S. A., & Pao, Y.-H. (1975). Numerical computation of turbulent shear flows. In F. N. Frenkiel and R. E. Munn (Eds.), *Advances in geophysics: Turbulent diffusion in environmental pollution, proceedings of a symposium held at Charlottesville, Virginia*. New York, NY: Academic.
Porté-Agel, F. (2004). A scale-dependent dynamic model for scalar transport in large-eddy simulations of the atmospheric boundary layer. *Boundary-Layer Meteorology*, *112*, 81–105. https://doi.org/10.1023/B:BOUN.0000020353.03398.20
Povitsky, A., & Morris, P. J. (2000). A higher-order compact method in space and time based on parallel implementation of the Thomas algorithm. *Journal of Computational Physics*, *161*, 182–203. https://doi.org/10.1006/jcph.2000.6497
Ramudu, E., Gelderloos, R., Yang, D., Meneveau, C., & Gnanadesikan, A. (2017). Replication data for: Large eddy simulation of heat entrainment under arctic sea ice. *Harvard Dataverse, 1*. https://doi.org/10.7910/DVN/OEZGXE
Ramudu, E., Hirsh, B. H., Olson, P., & Gnanadesikan, A. (2016). Turbulent heat exchange between water and ice at an evolving ice-water interface. *Journal of Fluid Mechanics*, *798*, 572–597.
Sharqawy, M. H., Lienhard, J. H., & Zubair, S. M. (2010). Thermophysical properties of seawater: A review of existing correlations and data. *Desalination and Water Treatment*, *16*(1–3), 354–380. https://doi.org/10.5004/dwt.2010.1079
Shaw, W. J., Stanton, T. P., McPhee, M. G., Morison, J. H., & Martinson, D. G. (2009). Role of the upper ocean in the energy budget of arctic sea ice during SHEBA. *Journal of Geophysical Research*, *114*, C06012. https://doi.org/10.1029/2008JC004991
Shimada, K., Kamoshida, T., Itoh, M., Nishino, S., Carmack, E., McLaughlin, F., . . . Proshutinsky, A. (2006). Pacific Ocean inflow: Influence on catastrophic reduction of sea ice cover in the Arctic Ocean. *Geophysical Research Letters*, *33*, L08065. https://doi.org/10.1029/2005GL025624
Simmonds, I., & Rudeva, I. (2012). The great Arctic cyclone of August 2012. *Geophysical Research Letters*, *39*, L23709. https://doi.org/10.1029/2012GL054259
Skyllingstad, E. D., & Denbo, D. W. (2001). Turbulence beneath sea ice and leads: A coupled sea ice/large-eddy simulation study. *Journal of Geophysical Research*, *106*(C2), 2477–2497. https://doi.org/10.1029/1999JC000091
Skyllingstad, E. D., Smyth, W. D., Moum, J. N., & Wijesekera, H. (1999). Upper-ocean turbulence during a westerly wind burst: A comparison of large-eddy simulation results and microstructure measurements. *Journal of Physical Oceanography*, *29*, 5–28. https://doi.org/10.1175/1520-0485(1999)029<0005:UOTDAW>2.0.CO;2

Smagorinsky, J. (1963). General circulation experiments with the primitive equations. I. The basic experiment. *Monthly Weather Review*, *91*(3), 99–164. https://doi.org/10.1175/1520-0493(1963)091<0099:GCEWTP>2.3.CO;2

Steele, M., Morison, J., Ermold, W., Rigor, I., Ortmeyer, M., & Shimada, K. (2004). Circulation of summer Pacific halocline water in the Arctic Ocean. *Journal of Geophysical Research*, *109*, C02027. https://doi.org/10.1029/2003JC002009

Steele, M., Zhang, J., & Ermold, W. (2010). Mechanisms of summertime upper Arctic Ocean warming and the effect on sea ice melt. *Journal of Geophysical Research*, *115*, C11004. https://doi.org/10.1029/2009JC005849

Stroeve, J., Holland, M. M., Meier, W., Scambos, T., & Serreze, M. (2007). Arctic sea ice decline: Faster than forecast. *Geophysical Research Letters*, *34*, L09501. https://doi.org/10.1029/2007GL029703

Timmermans, M.-L., Proshutinsky, A., Golubeva, E., Jackson, J. M., Krishfield, R., McCall, M., . . . Nishino, S. (2014). Mechanisms of Pacific Summer Water variability in the Arctic's Central Canada Basin. *Journal of Geophysical Research: Oceans*, *119*, 7523–7548. https://doi.org/10.1002/2014JC010273

Toole, J. M., Timmermans, M.-L., Perovich, D. K., Krishfield, R. A., Proshutinsky, A., & Richter-Menge, J. A. (2010). Influences of the ocean surface mixed layer and thermohaline stratification on Arctic Sea ice in the central Canada Basin. *Journal of Geophysical Research*, *115*, C10018. https://doi.org/10.1029/2009JC005660

UNESCO (1981). Tenth report of the Joint Panel on Oceanographic Tables and Standards (UNESCO Tech. Pap. in Mar. Sci. 36). Paris, France: UNESCO.

Woodgate, R. A., Aagaard, K., & Weingartner, T. J. (2006). Interannual changes in the Bering Strait fluxes of volume, heat and freshwater between 1991 and 2004. *Geophysical Research Letters*, *33*, L15609. https://doi.org/10.1029/2006GL026931

Woodgate, R. A., Weingartner, T., & Lindsay, R. (2010). The 2007 Bering Strait oceanic heat flux and anomalous Arctic sea-ice retreat. *Geophysical Research Letters*, *37*, L01602. https://doi.org/10.1029/2009GL041621

Yang, D., Chamecki, M., & Meneveau, C. (2014). Inhibition of oil plume dilution in Langmuir ocean circulation. *Geophysical Research Letters*, *41*, 1632–1638. https://doi.org/10.1002/2014GL059284

Yang, D., Chen, B., Chamecki, M., & Meneveau, C. (2015). Oil plumes and dispersion in Langmuir, upper-ocean turbulence: Large-eddy simulations and K-profile parameterization. *Journal of Geophysical Research: Oceans*, *120*, 4729–4759. https://doi.org/10.1002/2014JC010542

Zhang, J., Lindsay, R., Schweiger, A., & Steele, M. (2013). The impact of an intense summer cyclone on 2012 arctic sea ice retreat. *Geophysical Research Letters*, *40*, 720–726. https://doi.org/10.1002/grl.50190